

The shape of the dark matter halo in the early-type galaxy NGC 2974

Anne-Marie Weijmans^{1*}, Davor Krajnović², Glenn van de Ven^{3†},
Tom A. Oosterloo^{4,5}, Raffaella Morganti^{4,5} and P. T. de Zeeuw^{1,6}

¹ *Sterrewacht Leiden, Leiden University, Postbus 9513, 2300 RA Leiden, The Netherlands*

² *Denys Wilkinson Building, University of Oxford, Keble Road, Oxford, UK*

³ *Institute for Advanced Study, Einstein Drive, Princeton, NJ 08540, USA*

⁴ *Netherlands Foundation for Research in Astronomy, Postbus 2, 7990 AA Dwingeloo, The Netherlands*

⁵ *Kapteyn Astronomical Institute, University of Groningen, Postbus 800, 9700 AV Groningen, The Netherlands*

⁶ *European Southern Observatory, Karl-Schwarzschild Strasse 2, 85748 Garching bei Munchen, Germany*

2 November 2018

ABSTRACT

We present H I observations of the elliptical galaxy NGC 2974, obtained with the Very Large Array. These observations reveal that the previously detected H I disc in this galaxy (Kim et al. 1988) is in fact a ring. By studying the harmonic expansion of the velocity field along the ring, we constrain the elongation of the halo and find that the underlying gravitational potential is consistent with an axisymmetric shape.

We construct mass models of NGC 2974 by combining the H I rotation curve with the central kinematics of the ionised gas, obtained with the integral-field spectrograph SAURON. We introduce a new way of correcting the observed velocities of the ionised gas for asymmetric drift, and hereby disentangle the random motions of the gas caused by gravitational interaction from those caused by turbulence. To reproduce the observed flat rotation curve of the H I gas, we need to include a dark halo in our mass models. A pseudo-isothermal sphere provides the best model to fit our data, but we also tested an NFW halo and Modified Newtonian Dynamics (MOND), which fit the data marginally worse.

The mass-to-light ratio M/L_I increases in NGC 2974 from $4.3 M_\odot/L_{\odot,I}$ at one effective radius to $8.5 M_\odot/L_{\odot,I}$ at $5 R_e$. This increase of M/L already suggests the presence of dark matter: we find that within $5 R_e$ at least 55 per cent of the total mass is dark.

Key words: galaxies: elliptical and lenticular, cD — galaxies: individual: NGC 2974 — galaxies: kinematics and dynamics — galaxies: haloes — dark matter

1 INTRODUCTION

Although the presence of dark matter dominated haloes around spiral galaxies is well established (e.g. van Albada et al. 1985), there is still some controversy about their presence around early-type galaxies. Spiral galaxies often contain large regular H I discs, which allow us to obtain rotation curves out to large radii, and therefore we can constrain the properties of their dark haloes. But these discs are much rarer in elliptical galaxies (e.g. Bregman, Hogg & Roberts 1992), so that for this class of galaxies we are often required to use other tracers to obtain velocity measurements, such

as stellar kinematics, planetary nebulae or globular clusters. These tracers however are not available for all early-type galaxies, and give mixed results (e.g. Rix et al. 1997, Romanowsky et al. 2003, Bridges et al. 2006).

With the increase in sensitivity of radio telescopes, it has been discovered that many early-type galaxies in the field do contain H I gas, though with smaller surface densities than in spiral galaxies (e.g. Morganti et al. 2006). The average H I surface density in the Morganti et al. sample is around $1 M_\odot \text{ pc}^{-2}$, which is far below the typical value for spiral galaxies ($4 - 8 M_\odot \text{ pc}^{-2}$, e.g. Cayatte et al. 1994). This would explain why previously only the most gas-rich early-type galaxies were detected in H I. Morganti et al. find that H I can be present in different morphologies: H I discs

* E-mail: weijmans@strw.leidenuniv.nl

† Hubble Fellow

seem to be as common as off-set clouds and tails, though they occur mostly in the relatively gas-rich systems.

Recently rotation curves of H I discs in low surface brightness galaxies and dwarf galaxies, complemented with H α observations, have been used not only to confirm the existence of dark matter haloes, but also to obtain estimates on the inner slope of the density profiles of the haloes (e.g. van den Bosch et al. 2000; Weldrake, de Blok & Walter 2003). Simulations within a cold dark matter (CDM) cosmology yield haloes with cusps in their centres (NFW profiles, see Navarro, Frenk & White 1996), but observations suggest core-dominated profiles (e.g. de Blok & Bosma 2002; de Blok 2005).

Detailed studies of rotation curves of early-type galaxies that contain H I discs are sparser, due to lack of spatial resolution: to detect low H I surface densities, larger beams are needed. Also, only few early-type galaxies have H I discs that are extended and regular enough to allow for detailed studies. Comparing M/L values at large radii, derived from H I velocities, to M/L at smaller radii measured from ionised gas kinematics, the conclusion is that early-type galaxies also have dark matter dominated haloes (e.g. Bertola et al. 1993; Morganti et al. 1997; Sadler et al. 2000). Franx, van Gorkom & de Zeeuw (1994) used the H I ring of the elliptical galaxy IC 2006 to determine not only the mass, but also the shape of the dark halo. They concluded that IC 2006 is surrounded by an axisymmetric dark halo, using the geometry of the ring and an harmonic expansion of its velocity map.

In this paper, we present a similar analysis of the regularly rotating H I ring around the elliptical (E4) field galaxy NGC 2974. Kim et al. (1988) observed this galaxy before in H I but their data had lower spatial resolution than ours, and they found a filled disc instead of a ring. Cinzano & van der Marel (1994) found an embedded stellar disc in their dynamical model of this galaxy, based upon long-slit spectroscopic data, but Emsellem, Goudfrooij & Ferruit (2003) constructed a dynamical model of NGC 2974 based on TIGER integral-field spectrography and long-slit stellar kinematics, that does not require a hidden disc structure. They did report the detection of a two-arm gaseous spiral in the inner 200 pc of NGC 2974 from high resolution WFPC2 imaging. Krajnović et al. (2005) constructed axisymmetric dynamical models of both the stars and ionised gas based upon SAURON integral-field data. These models require a component with high angular momentum, consisting of a somewhat flattened distribution of stars, though not a thin stellar disc. Emsellem et al. (2007) classify NGC 2974 as a fast rotator, which means that it possesses large-scale rotation and that its angular momentum is well defined. Some of the characteristics of NGC 2974 are given in Table 1.

For our analysis of NGC 2974 we combine kinematics of neutral gas, obtained from our observations with the Very Large Array (VLA), with that of ionised gas, obtained with the integral-field spectrograph SAURON (Bacon et al. 2001). This combination of a small scale two-dimensional gas velocity map in the centre of the galaxy, and a H I velocity map at the outskirts, allows measurements of a rotation curve ranging from 100 pc within the centre of the galaxy to 10 kpc at the edges of the H I ring. We use this rotation curve, together with ground- and space based optical imaging, to determine the dark matter content in NGC 2974, and to constrain the shape of the dark halo.

Parameter	Value
Morphological Type	E4
M_B (mag)	-20.07
Effective $B - V$ (mag)	0.93
PA ($^\circ$)	41
Distance modulus (mag)	31.60
Distance (Mpc)	20.89
Distance scale (pc arcsec $^{-1}$)	101.3
Effective radius	24''

Table 1. Properties of NGC 2974. The values are taken from the Lyon/Meudon Extragalactic Database (LEDa) and corrected for the distance modulus, which is taken from the surface brightness fluctuation measurements by Tonry et al. (2001). Note that 0.06 mag is subtracted to adjust to the Cepheid zeropoint of Freedman et al. (2001); see Mei et al. (2005), section 3.3, for a discussion. The effective radius is taken from Cappellari et al. (2006).

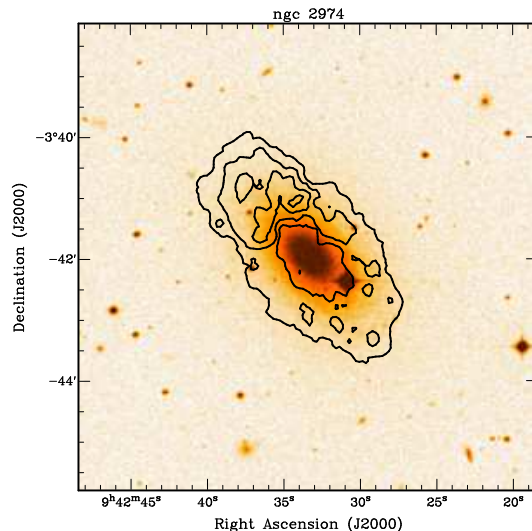


Figure 1. Total H I intensity contours superimposed onto the Digital Sky Survey optical image of NGC 2974. Contour levels are 1, 3, 5 and $7 \times 10^{20} \text{ cm}^{-2}$. The beamsize is 19.9×17.0 arcseconds.

In section 2, we discuss the two datasets and their reduction, and describe the H I ring. We concentrate on the analysis of the velocity maps in section 3. Section 4 is devoted to the rotation curve that we extract from the velocity maps, and in section 5 we show mass models with various halo models, and find the best fit to the rotation curve. Section 6 summarizes our results.

2 OBSERVATIONS AND DATA REDUCTION

2.1 VLA observations

Earlier VLA observations (Kim et al. 1988) of NGC 2974 showed that this galaxy contains a significant amount of H I that, in their observations, appears to be distributed in a regularly rotating disc. Given the modest spatial and velocity resolution of those observations, we re-observed NGC 2974 with the VLA C-array while also using a different frequency setup that allows us to study this galaxy at both

higher spatial and higher velocity resolution. The observations were performed on 11 and 19 September 2005 with a total on-source integration time of 15 hours. In each observation, two partially overlapping bands of 3.15 MHz and 64 channels were used. The two bands were offset by 500 km s^{-1} in central velocity. This frequency setup allows us to obtain good velocity resolution over a wide range of velocities (about 1080 km s^{-1}).

The data were calibrated following standard procedures using the MIRIAD software package (Sault, Teuben & Wright 1995). A spectral-line data cube was made using robust weighting (robustness = 1.0) giving a spatial resolution of $19.9'' \times 17.0''$ and a velocity resolution of 20.0 km s^{-1} (after Hanning smoothing). The noise in the final datacube is 0.23 mJy beam $^{-1}$.

To construct the total H I image, a mask was created using a datacube that was smoothed to about twice the spatial resolution and that was clipped at twice the noise of that smoothed datacube. The resulting total H I is shown in Figure 1, and our observations show that the H I is distributed in a regular rotating ring instead of a filled disc. The inner radius of the ring is approximately $50''$ (~ 5 kpc) and extends to $120''$, which corresponds to 12 kpc, or 5 effective radii ($1 R_e = 24''$).

The H I velocity field was derived by fitting Gaussians to the spectra at those positions where signal is detected in the total H I image. The resulting velocity map is shown in Figure 2. Typical errors on this map are 5 - 10 km s^{-1} .

We find a total mass of $5.5 \times 10^8 M_\odot$ for the H I gas content of the ring, which is in agreement with Kim et al. (1988), if we correct for the difference in assumed distance modulus. The amount and morphology of the H I observed in NGC 2974 are not unusual for early-type galaxies. Oosterloo et al. (2007) have found that between 5 and 10 per cent of early-type galaxies show H I masses well above $10^9 M_\odot$, while the fraction of detections increases further for lower H I masses (Morganti et al. 2006). The majority of the H I-rich systems have the neutral hydrogen distributed in disc/ring like structures (often warped) with low surface brightness density and no or little ongoing star formation, as observed in NGC 2974. However, there is a region in the North-East of the H I ring where the surface density is higher, and the gas could be forming stars. Jeong et al. (2007) published UV imaging of NGC 2974, obtained with GALEX. Their images reveal indeed a region of increased starformation in the North-East of the galaxy, as well as a starforming ring at the inner edges of the H I ring.

At least some of the most H I rich structures are the results of major mergers (see e.g. Serra et al. 2006). For the systems with less extreme H I masses, like NGC 2974, the origin of the gas is less clear. Accretion of small companions is a possibility, but smooth, cold accretion from the intergalactic medium (IGM) is an alternative scenario.

2.2 SAURON observations

Maps of the stellar and ionised gas kinematics of NGC 2974, obtained with the integral-field spectrograph SAURON were presented in Emsellem et al. (2004) and Sarzi et al. (2006), respectively, and we refer the reader to these papers for the methods of data reduction and extraction of the kinematics.

In Figure 2 we compare both the SAURON velocity maps

of stars and [O III] with the velocity map of the H I ring. Stars and gas are well aligned, and the transition between the ionised and the neutral gas seems to be smooth, suggesting that they form one single disc. The twist in the velocity map of the ionised gas in the inner $4''$ is likely caused by the inner bar of this galaxy (Emsellem et al. 2003, Krajnović et al. 2005).

3 ANALYSIS OF VELOCITY FIELDS

We used kinemetry (Krajnović et al. 2006) to analyse the SAURON and VLA velocity maps. In our application to a gas disc, kinemetry reduces to the tilted-ring method (Begeman 1978). The velocity along each elliptical ring is expanded in Fourier components (e.g. Franx et al. 1994; Schoenmakers, Franx & de Zeeuw 1997):

$$V_{\text{los}}(R, \phi) = V_{\text{sys}}(R) + \sum_{n=1}^N c_n(R) \cos n\phi + s_n(R) \sin n\phi, \quad (1)$$

where V_{los} is the observed velocity, R is the length of the semimajor axis of the elliptical ring, ϕ the azimuthal angle, measured from the projected major axis of the galaxy, V_{sys} the systemic velocity of the ring and c_n and s_n are the coefficients of the harmonic expansion. The c_1 term relates to the circular velocity V_c in the disc, so that $c_1 = V_c \sin i$, where i is the inclination of the gas disc. Assuming that motions in the ring are intrinsically circular and that the ring is infinitely thin, the inclination can be inferred from the flattening q of the fitted ellipse: $\cos i = q$.

If a gas disc only displays pure circular motions, all harmonic terms other than c_1 in Equation (1) are zero. Noncircular motions, originating from e.g. inflows caused by spiral arms or bars, or a triaxial potential, will cause these terms to deviate from zero. Alternatively, also wrong input parameters of the ring (which are flattening q , position angle Γ and the coordinates of the centre of the ellipse) will result in specific patterns in these terms, see e.g. van der Kruit & Allen (1978), Schoenmakers et al. (1997) and also Krajnović et al. (2006) for details. Therefore, the flattening and position angle of each ring are determined by minimising s_1 , s_3 and c_3 along that ring. The centre is kept constant and is chosen to coincide with the position of maximal flux in the galaxy.

3.1 Noncircular motions

Figure 3 shows the properties of the elliptic rings that were fitted to the SAURON and VLA velocity fields, and Figure 4 shows the resulting harmonic terms. The datapoints of the VLA data are separated by approximately one beamsizes. Error bars were calculated by constructing 100 Monte Carlo realisations of the velocity fields, where the measurement errors of the maps were taken into account.

Both the position angles and the inclinations of the rings show some variation in the SAURON field, but are very stable in the VLA field. The dashed line in the top two panels of Figure 3 indicates the mean value of the position angle and inclination of the H I data, which are $\Gamma = 47 \pm 1^\circ$ and $i = 60 \pm 2^\circ$. Here, Γ is the position angle of the receding

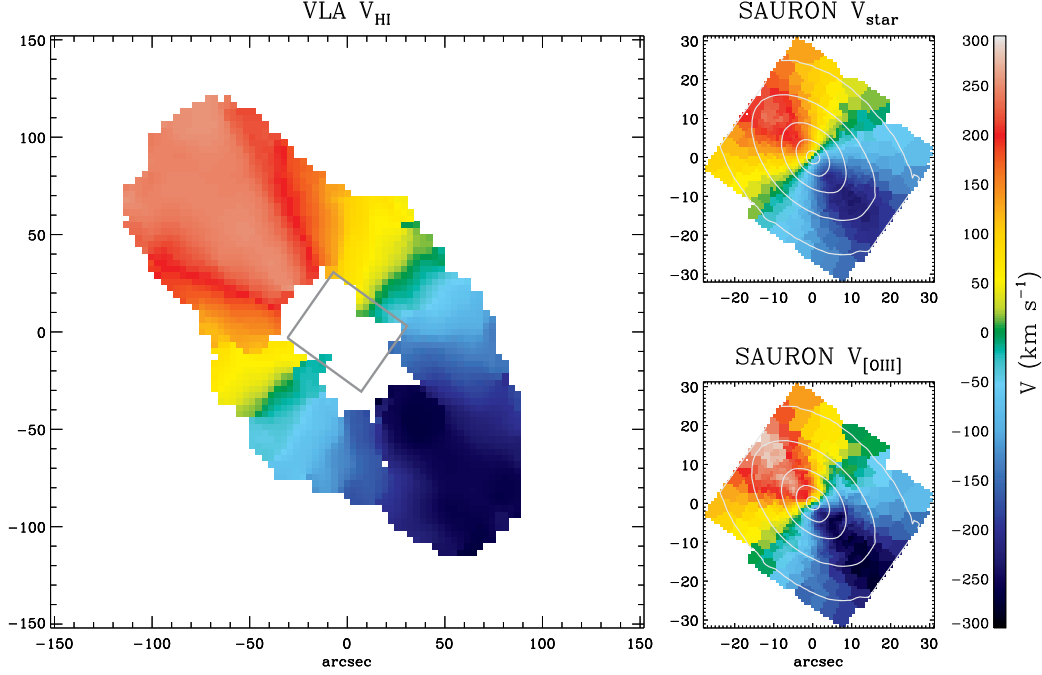


Figure 2. Velocity maps of the neutral hydrogen (VLA) and ionised gas and stars (SAURON) in NGC 2974. Both the stars and the neutral and ionised gas are well aligned. The maps are orientated so that North is up and East is to the left. The grey box in the VLA map encloses the SAURON fields shown at the right.

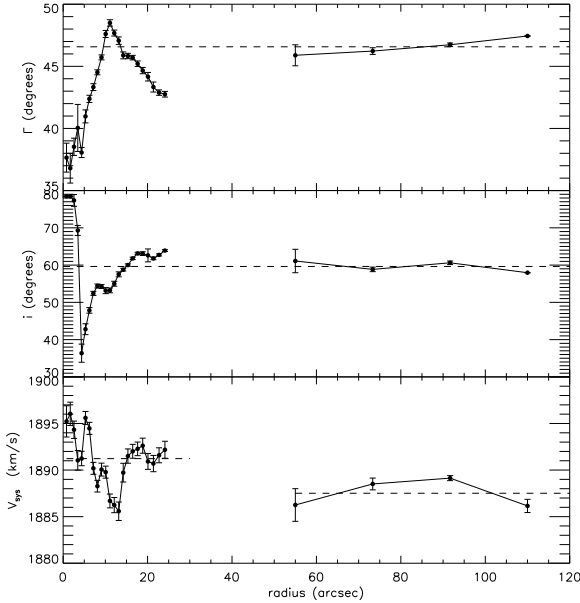


Figure 3. From top to bottom: position angle Γ , inclination i and systemic velocity of the rings that are fitted to the SAURON and VLA velocity fields of NGC 2974. The position angle indicates the receding side of the galaxy and is measured North through East. The dashed lines in the top two panels indicate the mean value of Γ and i generated by the H I rings. The bottom panel has two dashed lines, indicating the mean systemic velocity of the SAURON and VLA rings separately.

side of the galaxy, measured North through East. The systemic velocities (lower panel of Figure 3) have been corrected for barycentric motion and are in good agreement. For the SAURON field we find a systemic velocity of $1891 \pm 3 \text{ km s}^{-1}$, while for the VLA field we find $1888 \pm 2 \text{ km s}^{-1}$. The dashed lines give both these mean velocities. Both the inclination and the systemic velocity that we find are in agreement with previous studies (Cinzano & Van der Marel 1994, Emsellem et al. 2003, Krajnović et al. 2005).

The harmonic terms are shown in Figure 4. All terms are normalised with respect to c_1 . From c_1 we see that the velocity curve of the gas rises steeply in the centre, but flattens out at larger radii. This already suggests that a dark halo is present around this galaxy. In §4 we will analyse the rotation curve in more detail.

The other terms have small amplitudes, and are small compared to c_1 (< 4 per cent). We do not observe signatures that could indicate incorrect ring parameters, as described in Schoenmakers et al. (1997) and Krajnović et al. (2006).

3.2 Shape of the gravitational potential

Following Schoenmakers et al. (1997), we calculate the elongation of the potential from the harmonic terms. Using epicycle theory these authors showed that an $\cos m\phi$ -term perturbation of the potential results in signal in the $m - 1$ and $m + 1$ coefficients of the harmonic expansion in Equation (1).

We assume that the potential of NGC 2974 is affected by an $m = 2$ perturbation, which could correspond to a perturbation by a bar. We assume that the galaxy is not affected by lopsidedness, warps or spiral arms. To first order,

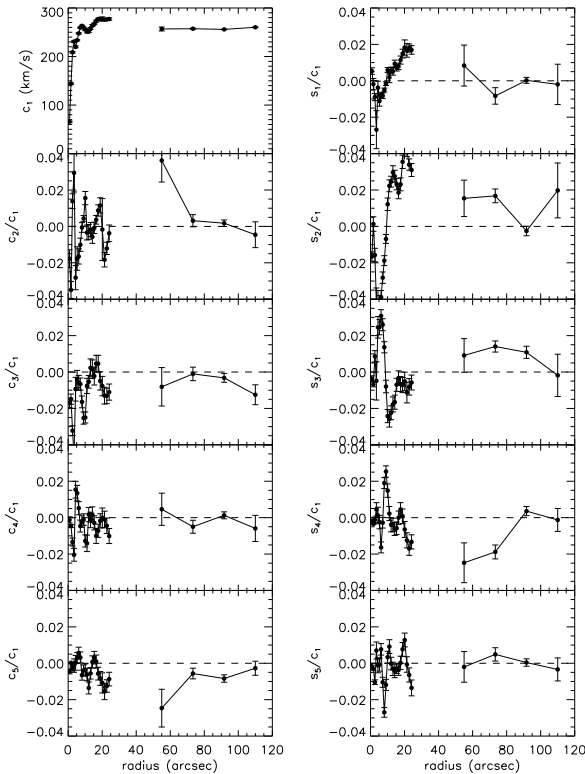


Figure 4. Coefficients of the harmonic expansion on the SAURON and VLA velocity fields. All except c_1 are normalized with respect to c_1 .

the potential of the galaxy in the plane of the gas ring can then be written as:

$$\Phi(R, \phi) = \Phi_0(R) + \Phi_2(R) \cos 2\phi, \quad (2)$$

with $\Phi_2(R) \ll \Phi_0(R)$. As explained in Schoenmakers et al. (1997), the elongation of the potential ϵ_{pot} in the plane of the gas is in this case given by:

$$\epsilon_{\text{pot}} \sin 2\varphi = \frac{(s_3 - s_1)}{c_1} \frac{(1 + 2q^2 + 5q^4)}{1 - q^4}, \quad (3)$$

where φ is one of the viewing angles of the galaxy, namely the angle between the minor axis of the galaxy and the observer, measured in the plane of the disc. This viewing angle is in general unknown, so that from this formula only a lower limit on the elongation can be derived. Schoenmakers (1998) used this method in a statistical way and found an average elongation $\epsilon_{\text{pot}} = 0.044$ for a sample of 8 spiral galaxies.

We calculated the elongation at different radii in NGC 2974, and the result is plotted in Figure 5. As in Schoenmakers et al, we did not fix Γ and q when determining the harmonic terms, because an offset in Γ or q introduces extra signal in c_1, s_1 and s_3 , that would then be attributed to the elongation of the potential.

Although the ionised gas has high random motions (see also § 4) and therefore the calculated elongation is probably only approximate, it is striking that the elongation changes sign around $10''$. The potential in the inner 10 arcseconds has a rather high elongation $\epsilon_{\text{pot}} \sin 2\varphi = 0.10 \pm 0.08$, while

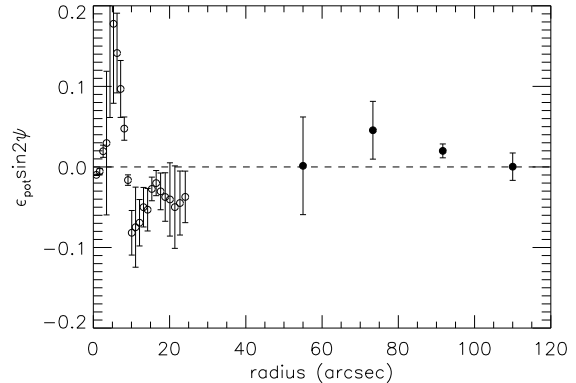


Figure 5. Elongation of the potential ($\epsilon_{\text{pot}} \sin 2\varphi$) of NGC 2974 as a function of radius. Open dots denote measurements from the ionised gas, filled dots represent the H I gas. The elongation as measured from the ionised gas is varying, due to the bar and high random motions of the gas. The cold neutral gas yields a more reliable value for the elongation, and shows that the potential is consistent with axisymmetry.

outside this region the elongation as measured from the ionised gas is $\epsilon_{\text{pot}} \sin 2\varphi = -0.047 \pm 0.020$. The change of sign could be the result of the bar system in NGC 2974, with the direction along which the potential is elongated changing perpendicularly. It is worth mentioning here that Krajnović et al. (2005) find a ring in the [O III] equivalent width map, with a radius of $9''$. Their data suggest also the presence of a (pseudo-)ring around $28''$, and Jeong et al. (2007) find a ring with a radius of $\sim 60''$ in their GALEX UV map, which is where our H I starts. Assuming that these three rings are resonances of a single bar, Jeong et al. (2007) deduce a pattern speed of $78 \pm 6 \text{ km s}^{-1} \text{ kpc}^{-1}$. In addition to the large scale bar, Emsellem et al. (2003) postulate a small nuclear bar ($\sim 3''$).

The H I gas is more suitable for measuring the elongation of the potential, since the cold gas has a small velocity dispersion (typical values $< 10 \text{ km s}^{-1}$) and is on nearly circular orbits. Taking the mean value of the elongation as obtained from the H I field, we find $\epsilon_{\text{pot}} \sin 2\varphi = 0.016 \pm 0.022$. We conclude that the potential of NGC 2974 is well approximated by an axisymmetric one.

4 ROTATION CURVE

To find the rotation curve of NGC 2974, we subtract the systemic velocities from the ionised and neutral gas velocity fields separately. Next, we fix $\Gamma = 47^\circ$ and $q = 0.50$ (or equivalently $i = 60^\circ$) of the ellipses to the mean values obtained from the neutral gas, and rerun kinemetry on both the velocity maps, now forcing the position angle and flattening to be the same everywhere in the gas disc. Also, because velocity is an odd moment, the even terms in the harmonic expansion should be zero, and are not taken into account during the fit (see Krajnović et al. 2006). The rotation curve of the ionised gas is shown in Figure 6 (open diamonds).

The ionised gas has a high observed velocity dispersion σ_{obs} , exceeding 250 km s^{-1} in the centre of the galaxy. Three

phenomena can contribute to the observed velocity dispersion of a gas: thermal motions, turbulence and gravitational interactions:

$$\sigma_{\text{obs}}^2 = \sigma_{\text{thermal}}^2 + \sigma_{\text{turb}}^2 + \sigma_{\text{grav}}^2. \quad (4)$$

The thermal velocity dispersion is always present, and caused by the thermal energy of the gas molecules:

$$\sigma_{\text{thermal}}^2 = \frac{kT}{m}, \quad (5)$$

where k is Boltzmann's constant, T the temperature of the gas and m the typical mass of a gas particle. The contribution of σ_{thermal} to the total velocity distribution in ionised gas is small: a typical temperature for ionised gas is 10^4 K, which implies $\sigma_{\text{thermal}} \sim 10$ km/s.

Turbulence can be caused by e.g. internal motions within the gas clouds or shocks induced by a non-axisymmetric perturbation to the potential, such as a bar. This increases the dispersion, but has a negligible effect on the circular velocity of the gas. In contrast, gravitational interactions of individual gas clouds not only increase random motions of the clouds and therefore their dispersion, but also lower the observed velocity. To correct for this last effect, we need to apply an asymmetric drift correction to recover the true circular velocity.

Unfortunately, it is not possible *a priori* to determine which fraction of the high velocity dispersion in the ionised gas is caused by turbulence and which by gravitational interactions. We therefore now first investigate the effect of asymmetric drift on the rotation curve of the ionised gas.

4.1 Asymmetric drift correction

Due to gravitational interactions of gas clouds on circular orbits, the observed velocity is lower than the circular velocity connected to the gravitational potential. Since we are interested in the mass distribution of NGC 2974, we need to trace the potential, and therefore we have to increase our observed velocity with an asymmetric drift correction, to obtain the true circular velocity. We follow the formalism described in Appendix A, which is based on the Jeans equations and the higher order velocity moments of the collisionless Boltzmann equation.

We assume that the galaxy is axisymmetric, which is a valid approach given the low elongation of the potential that we derived in section 3.2. Further we assume that the gas lies in a thin disc.

We fit the prescription that Evans & de Zeeuw (1994) used for their power-law models to the rotation curve extracted from the ionised gas,

$$v_{\text{mod}} = \frac{V_{\infty} R}{R_{\text{mod}}}, \quad (6)$$

where V_{∞} is the rotation velocity at large radii, and we introduce

$$R_{\text{mod}}^2 = R^2 + R_c^2, \quad (7)$$

with R_c the core radius of the model. This is Equation (A14) evaluated in the plane of the disc ($z = 0$), with a flat rotation curve at large radii ($\beta = 0$). Since we observe the gas only in the equatorial plane of the galaxy, we cannot constrain the

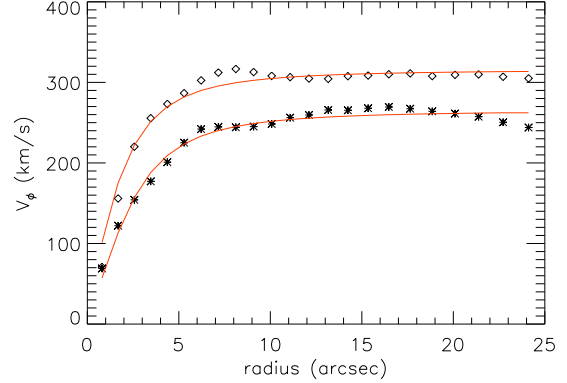


Figure 6. Rotation curves of the ionised gas (open diamonds) and stars (stars), together with their best fit power-law models (red curves). The rotation curves have been extracted from the SAURON velocity fields.

flattening of the potential q_{Φ} . We therefore assumed a spherical potential $q_{\Phi} = 1$, which is not a bad approximation even if the density distribution is flattened, since the dependence on q_{Φ} is weak. Moreover, even though the density distribution of most galaxies is clearly flattened, the potential is in general significantly rounder than the density. For example, an axisymmetric logarithmic potential is only about a third as flattened as the corresponding density distribution (e.g. §2.2.2 of Binney & Tremaine 1987).

To be able to fit the observed velocity we need to convolve our model with the point-spread function (PSF) of the observations, and take the binning into account that results from the finite pixel size of the CCD. We therefore constructed a two-dimensional velocity field of the extracted rotation curve, such that

$$V(R, \phi) = v_{\text{mod}} \cos \phi \sin i, \quad (8)$$

and we convolved this field with a kernel as described in the appendix of Qian et al. (1995). This kernel takes into account the blurring caused by the atmosphere and the instrument (FWHM = $1.4''$, for the SAURON observations of NGC 2974, see Emsellem et al. 2004) and the spatial resolution of the reduced observations ($0.8''$ for SAURON). We extracted the velocity along the major axis of the convolved velocity model and used the resulting rotation curve to fit our observations. The best fit is shown in Figure 6, and has a core radius $R_c = 2.1''$ (~ 0.2 kpc).

Under the assumptions of Equation (6), the asymmetric drift correction of Equation (A17) reduces to

$$V_c^2 = \overline{v_{\phi}^2} - \sigma_R^2 \left[\frac{\partial \ln \Sigma}{\partial \ln R} + \frac{\partial \ln \sigma_R^2}{\partial \ln R} + \frac{R^2}{2R_{\text{mod}}^2} + \frac{\kappa R^2}{\kappa(2R_{\text{mod}}^2 - R^2) + R^2} \right], \quad (9)$$

where $\overline{v_{\phi}^2}$ is the observed velocity, Σ is the surface brightness of the ionised gas and σ_R the radial dispersion of the gas. The last two terms in the equation are connected to the shape of the velocity ellipsoid, with κ indicating the alignment of the ellipsoid, see Appendix A.

To determine the slope of the surface brightness profile,

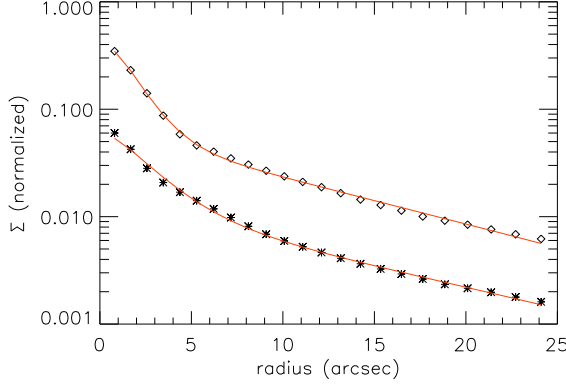


Figure 7. Profile and fit to the surface brightness of the ionised gas (diamonds) and to the stars (stars). Both profiles have been normalized, and the profile of the stellar surface brightness has been offset by a factor of 10, to distinguish it from the gaseous one.

we run kinemetry on the [O III] flux map, extracting the surface brightness along ellipses with the same position angle and flattening as the ones used to describe the velocity field. To decrease the noise we fit a double exponential function to the profile,

$$\Sigma(R) = \Sigma_0 e^{-R/R_0} + \Sigma_1 e^{-R/R_1}, \quad (10)$$

and determine the slope needed for the asymmetric drift correction from this parametrisation. The observed surface brightness profile and its fit are shown in Figure 7. As with the velocity profile, we convolved our model of the surface brightness during the fit with the kernel of Qian et al. (1995) to take seeing and sampling into account.

σ_R can be obtained from the observed velocity dispersion σ using Equation (A13). Along the major axis, and under the assumptions made above, this expression simplifies to

$$\sigma_{\text{obs}}^2 = \sigma_R^2 \left[1 - \frac{R^2 \sin^2 i}{2R_{\text{mod}}^2} - \frac{R^2 \cos^2 i}{\kappa R_{\text{mod}}^2 (2 - R^2/R_{\text{mod}}^2) + R^2} \right], \quad (11)$$

with R_{mod} defined in Equation (7), and adopting $R_c = 2.1''$ from the velocity profile.

We choose $\kappa = 0.5$, which is a typical value for a disc galaxy (e.g. Kent & de Zeeuw 1991), but we also experimented with other values for this parameter. Varying κ between 0 and 1 resulted in differences in V_c of approximately 10 km s^{-1} , and we adopt this value into the error bars of our final rotation curve.

To obtain the slope of σ_R we follow the same procedure as for the surface brightness, extracting the profile of σ_{obs} from the velocity dispersion map with kinemetry. We assume for the moment that turbulence is negligible in the galaxy ($\sigma_{\text{turb}} = 0$) and subtract quadratically $\sigma_{\text{thermal}} = 10 \text{ km s}^{-1}$ from σ_{obs} . We convert the resulting $\sigma_{\text{obs}} = \sigma_{\text{grav}}$ into σ_R using the relation in Equation (11). We parametrise this profile by

$$\sigma_R(R) = \sigma_0 + \sigma_1 e^{-R_{\text{mod}}/R_1}. \quad (12)$$

This profile has a core in the centre (introduced by R_{mod}), so that we can better reproduce the flattening of the profile

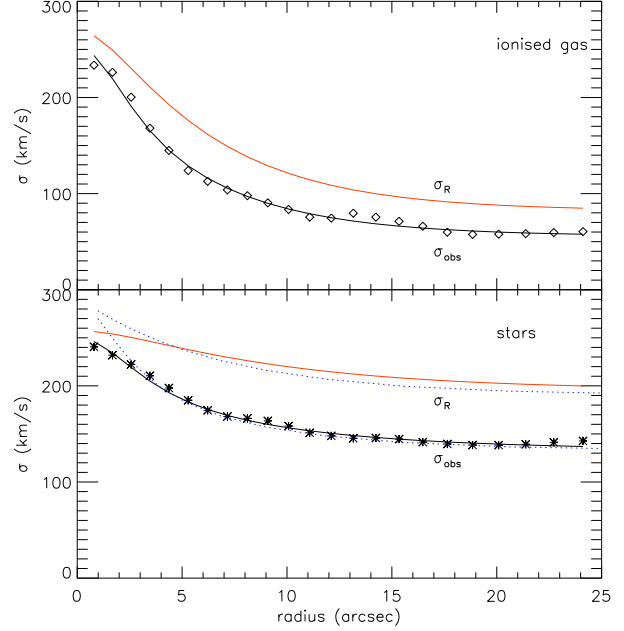


Figure 8. Top panel: observed velocity dispersion σ_{obs} of the ionised gas (black diamond) with its best fit (black line). The red line denotes the radial dispersion σ_R , calculated from the fit to σ_{obs} . Bottom panel: same as above, but now for the stellar observed velocity dispersion (black stars). The dotted blue lines represent σ_R and σ_{obs} as extracted from the Schwarzschild model of Krajnović et al. (2005).

towards the centre. Again, we convolved our model to take seeing and sampling into account during the fit. The top panel of Figure 8 shows the resulting profile and fit, as well as the observed velocity dispersion.

We first assume that turbulence plays no role in this galaxy, and we use σ_R as computed above to calculate the asymmetric drift correction (Equation 9). The resulting rotation curve, as well as the observed rotation curve of the ionised gas, is shown in the top panel of Figure 9.

To check our asymmetric drift corrected rotation curve of the ionised gas, we compare it with the asymmetric drift corrected stellar rotation curve. Stars do not feel turbulence and are not influenced by thermal motions like the gas, and therefore their observed velocity dispersion contains only contributions of gravitational interactions: $\sigma_{\text{obs}} = \sigma_{\text{grav}}$. If we are correct with our assumption that turbulence does not play a role in the ionised gas, then the stellar corrected rotation curve should overlap with the corrected curve of the gas. If it does not, then we know that we should not have neglected the turbulence.

To derive the asymmetric drift correction of the stars, we obtain the observed rotation curve, surface density and velocity dispersion of the stars from our SAURON observations with kinemetry, and parametrise them in the same way as we did for the ionised gas (see Figures 6 - 8 for the observed profiles and their models). The models were convolved during the fitting as described for the ionised gas. Because for the stars $\sigma_{\text{obs}} = \sigma_{\text{grav}}$ we do not need to subtract σ_{thermal} as we did for the ionised gas and hence can calculate σ_R directly from Equation (11), where we inserted a core radius $R_c = 3.0''$ from the stellar velocity model.

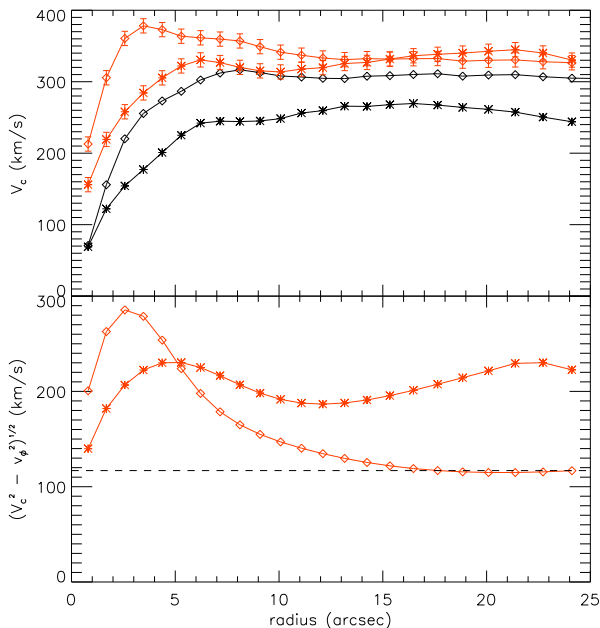


Figure 9. Top panel: observed rotation curve of the ionised gas (black diamonds) and stars (black stars) with their asymmetric drift corrected curve (red diamonds and stars). The correction to the ionised gas seems too high in the central part of the galaxy, when compared to the corrected stellar rotation curve. Bottom panel: asymmetric drift correction $(V_c^2 - v_\phi^2)^{1/2}$ of the ionised gas (diamonds) and the stars (stars). The dashed line denotes the mean asymmetric drift correction of the ionised gas outside 15 arcseconds.

In the above, we assumed that the stars lie in a thin disc, which is not the case in NGC 2974. To check the validity of our thin disc approximation for our model of σ_R , we extract this quantity from the Schwarzschild model of Krjnović et al. (2005), for $\theta = 84^\circ$, close to the $z = 0$ plane. The resulting profile is smoothed and shown as the upper dotted blue line in Figure 8. It is not a fit to the data, but derived independently from the Schwarzschild model, and agrees very well with the stellar σ_R we got from kinemetry. Also, σ_{obs} derived from the Schwarzschild model (lower dotted blue line) agrees with the results from kinemetry, giving us confidence that our stellar σ_R is reliable.

When we compare the asymmetric drift corrected rotation curves of the ionised gas and of the stars in Figure 9, then it is clear that although for $R > 15''$ the agreement between the curves is very good, the correction for the gas is too high in the central part of the galaxy. This is an indication that turbulence cannot be neglected here, and needs to be taken into account.

4.2 Turbulence

For radii larger than $15''$, the corrected velocity curve of the ionised gas is in agreement with the stellar corrected velocity curve, and since stellar motions are not influenced by turbulence, we can conclude that in this region turbulence is negligible. The bottom panel of Figure 9 shows the asymmetric drift correction $(V_c^2 - v_\phi^2)^{1/2}$ itself, and we see that outside $15''$, the correction is more or less constant at approximately 120 km s^{-1} (dashed line). In order to remove

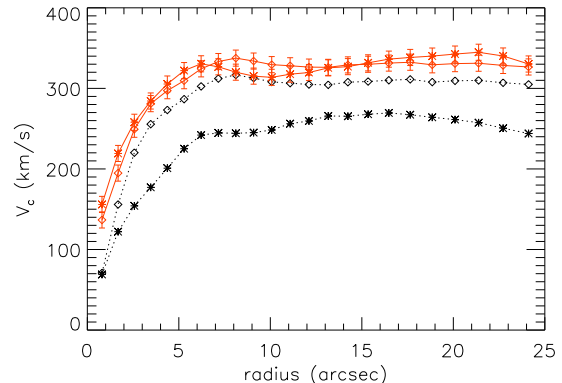


Figure 10. Asymmetric drift corrected rotation curve of the gas (red diamonds), removing turbulence as described in the text. The red stars denote the asymmetric drift corrected rotation curve of the stars. The two curves agree very well, suggesting that our turbulence model is adequate for our purposes. For comparison, also the observed rotation curves of the gas and stars are plotted (black diamonds and stars, respectively).

the turbulence from the central region in NGC 2974, we now assume that the asymmetric drift correction has the same value everywhere in the galaxy, namely 120 km s^{-1} . We add this value quadratically to the observed rotation curve of the ionised gas, and obtain the rotation curve shown in Figure 10. This corrected rotation curve agrees strikingly well with the corrected rotation curve of the stars, and this is a strong indication that our model for turbulence is reasonable, and at least good enough to get a reliable rotation curve for the ionised gas.

We now investigate the random motions resulting from turbulence and gravitational interaction in some more detail. Since we assumed a constant asymmetric drift correction $(V_c^2 - v_\phi^2)^{1/2}$ of $\sim 120 \text{ km s}^{-1}$, we can at each radius calculate the corresponding σ_R with Equation (9). Using Equation (11) we obtain the observed velocity dispersion, which in this case consists only of σ_{grav} . Since we know σ_{obs} , we can subtract quadratically σ_{grav} and $\sigma_{\text{thermal}} = 10 \text{ km s}^{-1}$ to obtain σ_{turb} .

Figure 11 shows σ_{obs} (deconvolved model) and its components σ_{thermal} , σ_{grav} and σ_{turb} . We fitted a single exponential function (Equation 10) with $R_c = 2.1''$ to the inner 15 arcseconds of σ_{turb} and find that with this parametrisation we can get a decent fit. We find a lengthscale of $5.0''$ for the turbulence. The fit is also shown in Figure 11.

5 MASS MODEL AND DARK MATTER CONTENT

In this section we combine the corrected rotation curve of the ionised gas with the rotation curve of the neutral gas. The rotation curve of NGC 2974 rises quickly to a maximal velocity and then declines to a somewhat lower velocity, after which it flattens out (see e.g. Figure 15). Unfortunately, we lack the data to study this decline in more detail, because our H I ring is not filled. The behaviour of our rotation curve is similar to what is seen in other bright galaxies with a concentrated light distribution (Casertano & van Gorkom 1991,

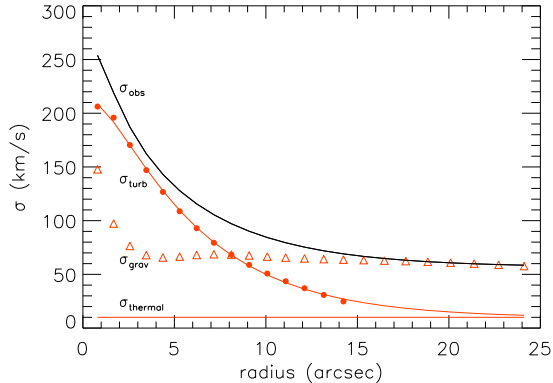


Figure 11. Observed deconvolved velocity dispersion (solid black line), with its components σ_{thermal} (red horizontal line), σ_{grav} (open red triangles) and σ_{turb} (filled red dots). An exponential fit to σ_{turb} is overplotted.

Noordermeer et al. 2007). The decline of the rotation curve in such systems could indicate that the mass distribution in the centre is dominated by the visible mass and that the dark halo only takes over at larger radii. In contrast, in galaxies where the light distribution is less concentrated, such as low-luminosity later-type galaxies, the rotation curves does not decline (e.g. Spekkens & Giovanelli 2006, Catinella, Giovanelli & Haynes 2006).

We separately model the contribution of the stars, neutral gas and dark halo to the gravitational potential. Also we derive the total mass-to-light ratio as a function of radius, and obtain a lower limit on the dark matter fraction in NGC 2974.

In our model, we do not take the weak bar system of NGC 2974 into account. Emsellem et al. (2003) find that the perturbation of the gravitational potential caused by the inner bar in their model of this galaxy is less than 2 per cent. Also, we find that the harmonic coefficients that could be influenced by a large scale bar (s_1 , s_3 and c_3) are small compared to the dominant term c_1 (< 4 per cent). We therefore conclude that although the rotation curve probably is affected by the presence of the bar system, this effect is small, and negligible compared to the systematic uncertainties introduced by the asymmetric drift correction. Furthermore, the largest constraints in our models come from the rotation curve at large radii, where we showed that the elongation of the potential is consistent with axisymmetry.

5.1 Stellar contribution

The contribution of the stellar mass to the gravitational potential and the corresponding circular velocity can be obtained by deprojecting and modelling the surface photometry of the galaxy. We use the Multi-Gaussian Expansion (MGE) method for this purpose, as described in Cappellari (2002).

Krajnović et al. (2005) presented an MGE model of NGC 2974, based upon the PC part of a dust-corrected WFPC2/F814W image and a ground-based *I*-band image obtained at the 1.0m Jacobus Kapteyn Telescope (JKT). This image was however not deep enough to yield an MGE

	HST/WFPC2	MDM
Filter Band	F814W	<i>I</i>
Exposure Time (s)	250	1500
Field of View	32'' × 32''	17.4' × 17.4'
Pixel scale (arcsec)	0.0455	0.508
Date of Observation	16 April 1997	26 March 2003

Table 2. Properties of the space- and ground-based imaging of NGC 2974, used to model the stellar contribution to the potential. The MDM image was constructed of 3 separate exposures, resulting in a total integration time of 1500 s.

model that is reliable out to $5 R_e$ or $120''$, which is the extent of our rotation curve. We therefore construct another MGE model, replacing the JKT *I*-band image with a deeper one obtained with the 1.3-m McGraw-Hill Telescope at the MDM Observatory (see Table 2). This image is badly contaminated by a bright foreground star, so we do not include the upper half of the image in the fit. Since our model is axisymmetric, enough signal remained to get a reliable fit. We also exclude other foreground stars and bleeding from the image. The parameters of the point spread function (PSF) for the WFPC2 image were taken from Krajnović et al. (2005).

We match the ground-based MDM image to the higher resolution WFPC2 image, and use it to constrain the MGE-fit outside $15''$. Outside $200''$, the signal of the galaxy dissolves into the background and we stop the fit there. We are therefore confident of our MGE model out to a radius of at least $120''$, which is the extent of the observed H I rotation curve. The goodness of fit can be examined as a function of radius in Figure 12.

We forced the axial ratios q_j of the Gaussians to lie in the interval $[0.58, 0.80]$ (which is the same range as Krajnović et al. (2005) used in their paper), maximising the number of allowed inclinations and staying as close as possible to a model with constant ellipticity, without significantly increasing the χ^2 of the fit. This resulted in an MGE model consisting of twelve Gaussians, whose parameters can be found in Table 3. The parameters of the inner Gaussians agree very well with the ones in Krajnović et al.'s model, which is not surprising as we used the same dust-corrected WFPC image. The outer Gaussians deviate, where their JKT image is replaced by our MDM image.

Figure 13 shows the WFPC2 and MDM photometry and the overlaid contours of the MGE model. Also shown is the masked MDM image. The deviations in the WFPC plot between the isophotes and the MGE model around $10''$ are point-symmetric and therefore probably reminiscent of a spiral structure (e.g. Emsellem et al. 2003). The deviations are however small, and we conclude that the MGE model is a good representation of the galaxy surface brightness.

5.2 Gas contribution

The contribution of the H I ring to the gravitational potential is small compared to the stars and halo ($5.5 \times 10^8 M_\odot$, three orders of magnitude smaller than the stellar mass) but still included in our mass models. We include a factor 1.3 in mass to account for the helium content of the ring. The mass

j	$I_j (L_\odot \text{ pc}^{-2})$	$\sigma_j \text{ (arcsec)}$	q_j	$L_j (\times 10^9 L_\odot)$
1	187628.	0.0376306	0.580000	0.0099
2	44798.9	0.0923231	0.800000	0.0197
3	25362.4	0.184352	0.800000	0.0445
4	28102.0	0.343100	0.586357	0.1251
5	23066.0	0.607222	0.722855	0.3964
6	9694.88	1.20984	0.774836	0.7089
7	5019.87	3.56754	0.659952	2.7186
8	1743.48	9.23267	0.580000	5.5578
9	329.832	16.9511	0.770081	4.7057
10	111.091	30.5721	0.580000	3.8829
11	96.2559	44.0573	0.717554	8.6440
12	16.7257	103.085	0.800000	9.1678

Table 3. Parameters of the Gaussians of the MGE model of NGC 2974. From left to right: number of the Gaussian, central intensity, width (standard deviation), axial ratio and total intensity.

of the ionised gas is estimated at only $2.2 \times 10^5 M_\odot$ (Sarzi et al. 2006), and therefore can be neglected in our models.

5.3 Mass-to-light ratio

By comparing the observed rotation curve and the light distribution from the MGE model, we can already calculate the mass-to-light ratio in NGC 2974. The enclosed mass within a certain radius r in a spherical system follows directly from the circular velocity:

$$M(< r) = \frac{V_c^2 r}{G}, \quad (13)$$

with G the gravitational constant. Here we assume that the gravitational potential of the total galaxy is spherical symmetric. This is clearly not the case for the neutral gas, which resides in a thin disc. However, the total mass of the gas is three orders of magnitudes smaller than the total mass, and therefore can be neglected. Also, the stars reside in a flattened potential, as can be shown from their MGE model. But since we cannot disentangle the contributions of the stars and the dark matter to the observed rotation velocity *a priori*, we will for the moment assume that also the stellar mass density can be approximated by a spherical distribution.

Since we know the mass within a sphere of radius r , we also need to calculate the enclosed I -band luminosity within a sphere. We first obtain the gravitational potential of our MGE model as a function of radius (see appendix A of Cappellari et al. 2002). Here, we take the flattening of the separate Gaussians into account. We subsequently calculate the corresponding circular velocity, with an arbitrary M_*/L . To find the luminosity enclosed in a sphere we calculate the spherical mass needed to produce this circular velocity with Equation (13), and convert this mass back to a luminosity using the same M_*/L that we used to calculate the velocity curve. This way we have replaced the luminosity within a flattened axisymmetric ellipsoid (oblate sphere) by a sphere with radius equal to the long axis of the ellipsoid.

With this method we arrive at a mass-to-light ratio $M/L_I = 8.5 M_\odot/L_{\odot,I}$ at 5 effective radii ($1R_e = 24''$). In the literature, this value is usually expressed in B -band

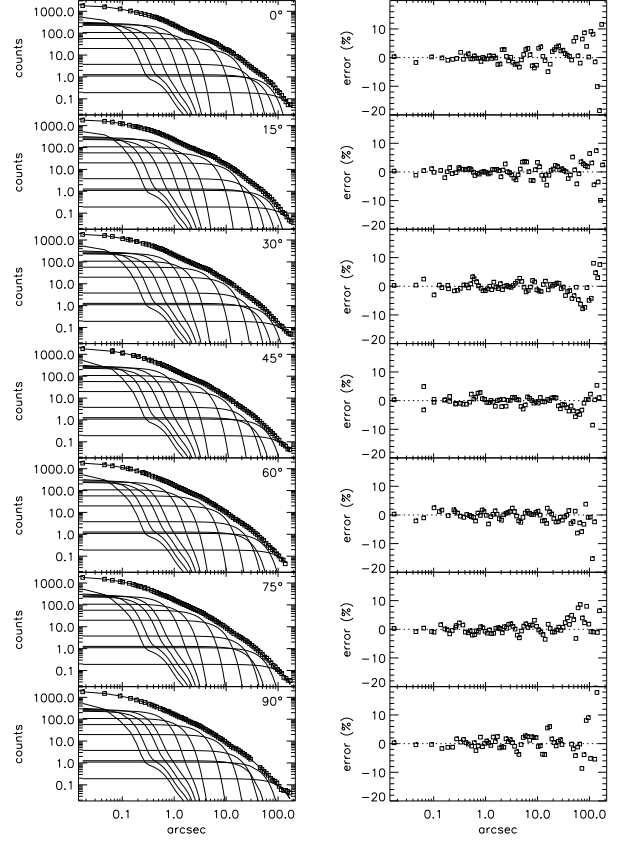


Figure 12. Left panels: comparison between the WFPC2 and MDM photometry (open squares) and the convolved Gaussians composing the MGE model of NGC 2974 (solid line), as a function of radius. Different panels show different angular sectors. Right panels: relative error of the MGE model compared to the data, as a function of radius.

luminosities. Using an absolute magnitude of $M_B = -20.07$ for NGC 2974 (see Table 1), we find that $M/L_B = 14 M_\odot/L_{\odot,B}$. We checked that M_B is consistent with our MGE model, adopting a colour $B - I = 2.13$ for NGC 2974 (see Tonry et al. 2001 and Table 1). H I studies of other early-type galaxies yield similar numbers (Morganti et al. 1997 and references therein). For example, Franx et al. (1994) find $M/L_B = 16 M_\odot/L_{\odot,B}$ at $6.5 R_e$ using the H I ring around IC 2006, and Oosterloo et al. (2002) report $M/L_B = 18 M_\odot/L_{\odot,B}$ for NGC 3108 at $6 R_e$.

Figure 14 shows the increase of M/L_I with radius. We find that within $1 R_e$, $M/L_I = 4.3 M_\odot/L_{\odot,I}$, which agrees with the results from Schwarzschild modeling of Krajnović et al. (2005) and Cappellari et al. (2006). The increase of M/L indicates that the fraction of dark matter grows towards larger radii.

5.4 Dark matter fraction

To calculate the dark matter fraction, we need to know the stellar mass-to-light ratio M_*/L . An upper limit on M_*/L_I can be derived by constructing a maximal disc model. From the MGE model we calculate a rotation curve (taking the flattening of the potential into account, as in Cappellari et al. 2002), and we increase M_*/L_I until the calculated curve

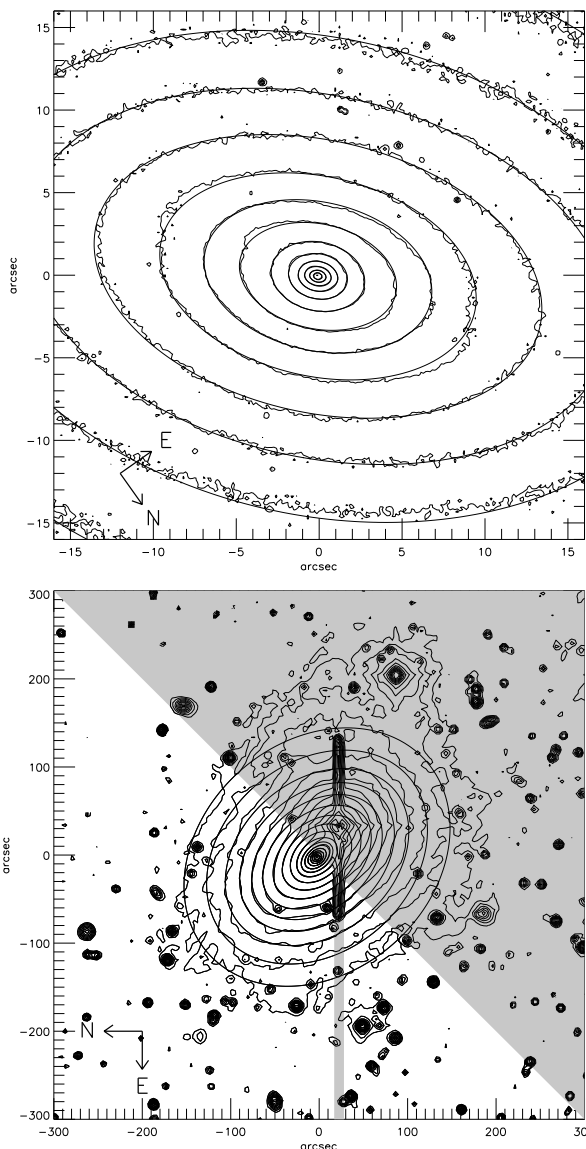


Figure 13. Contour maps of the I -band photometry of NGC 2974. From top to bottom: dust-corrected PC of WFPC2/F814W image and MDM image. The grey area in the MDM image indicates the area that has been excluded from the fit, because of contamination by the bright foreground star. Apart from this area, other foreground star were also masked during the fit. Overplotted are the contours of the MGE surface brightness model, convolved with the PSF of WFPC2.

exceeds the observed rotation curve. This way, we find that M_*/L_I cannot be larger than $3.8 M_\odot/L_{\odot,I}$. We plotted the rotation curve of the maximal disc model, together with the observed rotation curve in Figure 15. The rotation curve of the model has been convolved to take seeing and the resolution of the observations into account, as described in § 4.1. The contribution of the neutral gas to the gravitational potential has been included in the model, but has only a negligible effect on the fit.

It is clear that even in the maximal disc model, a dark matter halo is needed to explain the flat rotation curve of the H I gas at large radii. From this model, we can calculate a lower limit to the dark matter fraction in NGC 2974. We

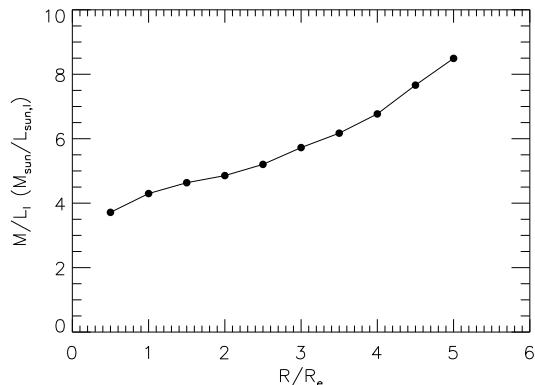


Figure 14. M/L_I as a function of radius. The increase of M/L_I is a strong indication for a dark matter halo around NGC 2974.

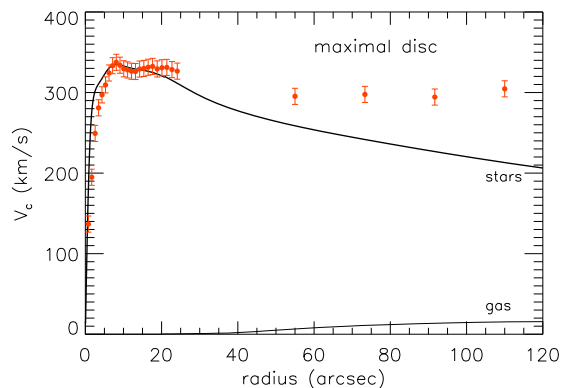


Figure 15. Best fit of a maximal disc model to the observed rotation curve. Red points indicate the observations and the thick black curve is the fit to these datapoints. This curve is calculated from the combined stellar and gaseous mass, and convolved with a kernel that takes seeing and sampling into account. The stellar mass-to-light ratio in this model is $3.8 M_\odot/L_{\odot,I}$.

then find that within one R_e , 12 per cent of the total mass is dark, while within $5 R_e$, this fraction has grown to 55 per cent.

There is however no reason to assume that the stellar mass-to-light ratio is well represented by its maximal allowed value. Cappellari et al. (2006) find $M_*/L_I = 2.34 M_\odot/L_{\odot,I}$ for NGC 2974, measured from line-strength values using single stellar population models. The formal error that they report on this mass-to-light ratio is ~ 10 per cent, but they warn that this value is strongly assumption dependent. Secondary star formation in a galaxy can result in an underestimation of M_*/L , and the GALEX observations of Jeong et al. (2007) indeed show evidence for recent star formation in NGC 2974. The population models of Cappellari et al. (2006) are based on a Kroupa initial mass function (IMF), but if instead a Salpeter IMF is used, their M_*/L_I values increase by ~ 40 per cent, which for NGC 2974 would result in $M_*/L_I = 3.3 M_\odot/L_{\odot,I}$. Cappellari et al. (2006) discard the Salpeter IMF based models, because for a large part

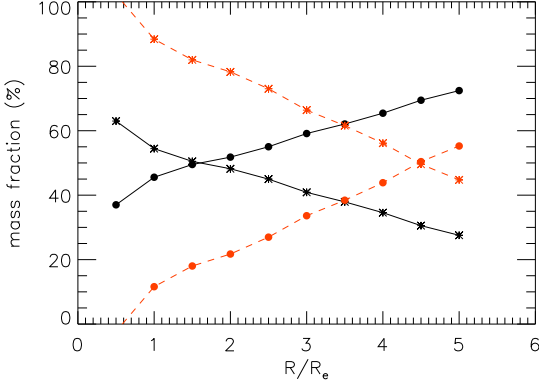


Figure 16. Dark matter fraction (filled dots) and stellar mass fraction (stars). The black solid lines assume a stellar M/L_I of $2.34 M_\odot/L_{\odot,I}$ as predicted by single stellar population models of NGC 2974. The red dashed lines provide lower and upper limits for the dark matter and stellar mass fraction, respectively, and are based on $M_*/L_I = 3.8 M_\odot/L_{\odot,I}$, from the maximal disc model.

of their sample their models then have $M_*/L_I > M_{\text{tot}}/L_I$, which is unphysical.

If we adopt $M_*/L_I = 2.34 M_\odot/L_{\odot,I}$ from the stellar population models, then 46 per cent of the total mass within $1 R_e$ is dark. The dark matter fraction increases to 72 per cent within $5 R_e$. See Figure 16 for the change in dark matter fraction as a function of radius, and the comparison with the lower limits derived above.

Gerhard et al. (2001) and Cappellari et al. (2006) find an average dark matter fraction of ~ 30 per cent within one effective radius in early-type galaxies, but we note that NGC 2974 is an outlier in the sample of Cappellari et al. The value of 47 per cent that we find is a bit high compared to this average, though the minimal fraction of dark matter is 14 per cent in our galaxy. Without an accurate determination of M_*/L we can not give a more precise estimate on the dark matter fraction in NGC 2974.

5.5 Halo models

We now include a dark halo in our model, to explain the flat rotation curve that we extracted from the H I ring. We explore two different halo models: the pseudo-isothermal sphere and the NFW profile.

The pseudo-isothermal sphere has a density profile given by:

$$\rho(r) = \frac{\rho_0}{1 + (r/r_c)^2}, \quad (14)$$

where ρ_0 is the central density of the sphere, and r_c is the core radius.

The velocity curve resulting from the density profile of the pseudo-isothermal sphere is straightforward to derive analytically, and given by

$$V_c^2(r) = 4\pi G \rho_0 r_c^2 \left(1 - \frac{r_c}{r} \arctan \frac{r}{r_c} \right). \quad (15)$$

The NFW profile was introduced by Navarro et al. (1996) to describe the haloes resulting from simulations,

taking a cold dark matter cosmology into account. This profile has a central cusp, in contrast to the pseudo-isothermal sphere which is core-dominated. Its density profile is given by

$$\rho(r) = \frac{\rho_s}{r/r_s \left[1 + \left(\frac{r}{r_s} \right)^2 \right]}, \quad (16)$$

with ρ_s the characteristic density of the halo and r_s a characteristic radius. The velocity curve of the NFW halo is given by

$$V_c^2(r) = V_{200}^2 \frac{\ln(1+cx) - cx/(1+cx)}{x[\ln(1+cx) - c/(1+cx)]}, \quad (17)$$

where $x = r/r_{200}$ and c the concentration parameter defined by $c = r_{200}/r_s$. r_{200} is defined such that within this radius the mean density is 200 times the critical density ρ_{crit} , and V_{200} is the circular velocity at that radius. These parameters depend on the assumed cosmology.

We construct mass models of NGC 2974 including a dark matter halo with the observed stellar and gaseous mass. We then calculate the circular velocity resulting from our models, by adding the circular velocities resulting from the separate components:

$$V_c^2(r) = V_{c,\text{halo}}^2 + V_{c,\text{stars}}^2 + V_{c,\text{gas}}^2, \quad (18)$$

and fit these to our observed rotation curve. The inner $25''$ of our model rotation curve, which are based on the SAURON ionised gas measurements, are convolved with a kernel to take seeing and sampling into account, as described in § 4.1.

For both profiles, we found that we could not constrain the stellar mass-to-light ratio in our models because of degeneracies: for each M_*/L_I below the maximal disc value of $3.8 M_\odot/L_{\odot,I}$ we could get a decent fit. We therefore show two fits for each model, with M_*/L values that are justified by either linestrength measurements and single stellar population models ($M_*/L_I = 2.34 M_\odot/L_{\odot,I}$) or the observed rotation curve itself ($M_*/L_I = 3.8 M_\odot/L_{\odot,I}$). This last case would be a model requiring a minimal halo.

The best fit models for a dark halo described by a pseudo-isothermal sphere is shown in Figure 17. The model in the top panel has a fixed $M_*/L_I = 2.34 M_\odot/L_{\odot,I}$, while the bottom panel shows the model with $M_*/L_I = 3.8 M_\odot/L_{\odot,I}$. The first model fits the SAURON measurement of the rotation curve well, but has a small slope at the outer part, where the observations show a flat rotation curve. Nevertheless, this model provides a good fit, with a minimal $\chi^2 = 27$ for $27 - 2 = 25$ degrees of freedom. We find for this model $\rho_0 = 19 M_\odot \text{ pc}^{-3}$ and core radius $r_c = 2.3'' = 0.23$ kpc. The second model with $M_*/L_I = 3.8 M_\odot/L_{\odot,I}$ provides a better fit to the H I measurements, but has problems fitting the central part of the rotation curve. The model has a lower central density $\rho_0 = 0.06 M_\odot \text{ pc}^{-3}$ and larger core radius $r_c = 54'' = 5.4$ kpc. The fit is worse than for the previous model, with $\chi^2 = 133$.

Figure 18 shows the best fitting-models with an NFW dark halo. This model fits the data less well than the pseudo-isothermal sphere: for the model with $M_*/L_I = 2.34 M_\odot/L_{\odot,I}$ (top panel) we find a minimal $\chi^2 = 44$ for $27 - 2$ degrees of freedom. The corresponding parameters of the density function are $\rho_s = 1.1 M_\odot \text{ pc}^{-3}$ and $r_s = 21'' = 2.1$ kpc. For $M_*/L_I = 3.8 M_\odot/L_{\odot,I}$ the fit is worse ($\chi^2 = 144$) but the outer part of the rotation curve is better fitted. We

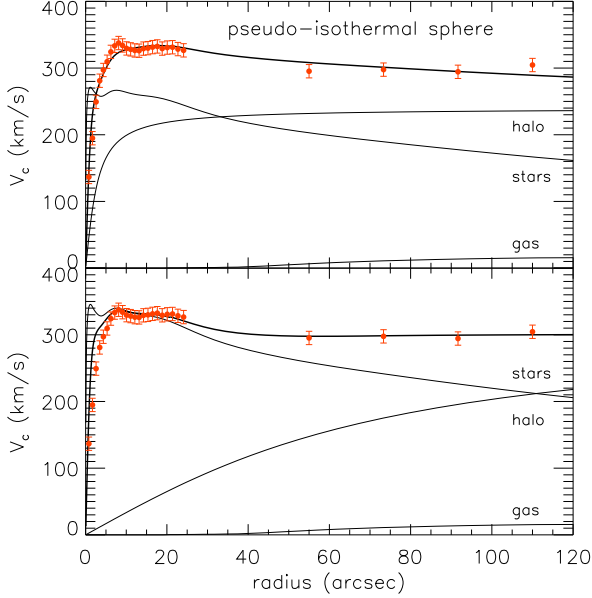


Figure 17. Best fit models of a dark halo represented by a pseudo-isothermal sphere. The top panel has a stellar M_*/L_I of $2.34 M_\odot/L_{\odot,I}$ from stellar population models, and the bottom panel has $M_*/L_I = 3.8 M_\odot/L_{\odot,I}$ from the maximal disc model. The red dots are our observations from the ionised gas (asymmetric drift corrected) and H I gas. The rotation curves resulting from the potentials of the halo, stars and gas are plotted separately, where the first two are unconvolved. The bold line denotes the fit to the data, and is the convolved rotation curve resulting from the combined potential of halo, stars and gas.

find $\rho_s = 1.1 \times 10^{-3} M_\odot \text{ pc}^{-3}$ and $r_s \approx 1300''$, which corresponds to approximately 130 kpc.

Adopting $H_0 = 73 \text{ km s}^{-1} \text{ Mpc}^{-1}$, the critical density is given by $\rho_{\text{crit}} = 3H_0^2/8\pi G = 1.5 \times 10^{-7} M_\odot \text{ pc}^{-3}$. We calculate the concentration parameter c , given that

$$\frac{\rho_s}{\rho_{\text{crit}}} = \frac{200}{3} \frac{c^3}{\ln(1+c) - c/(1+c)}, \quad (19)$$

and find $c = 71$ and $c = 4.7$ for the NFW profiles in the $M_*/L_I = 2.34 M_\odot/L_{\odot,I}$ and $M_*/L_I = 3.8 M_\odot/L_{\odot,I}$ models, respectively. These values are quite deviant from the value that is expected from cosmological simulations ($c \sim 10$, Bullock et al. 2001). When fixing $c = 10$ and fitting again an NFW halo to our observations with M_*/L_I and the scale radius as free parameters, we arrive at the model shown in Figure 19. We find $M_*/L_I = 3.3 M_\odot/L_{\odot,I}$ and $r_s \approx 380'' \approx 38 \text{ kpc}$, with a minimal χ^2 value of 87 for 27 – 2 degrees of freedom. We regard this model as more realistic than the two other NFW profiles mentioned above, but since also here the fit is not perfect, we cannot conclude that therefore $M_*/L_I = 3.3 M_\odot/L_{\odot,I}$ is a better estimate for the stellar mass-to-light ratio in NGC 2974, than the value from the stellar population models.

The results of the halo models discussed above are summarized in Table 4.

5.6 MOND

An alternative to including a dark matter halo in a galaxy to explain its rotation curve at large radii, is provided by

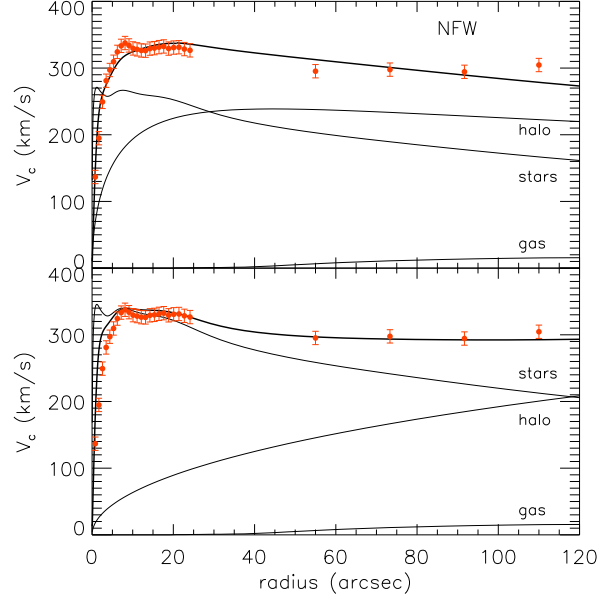


Figure 18. Same as Figure 17, but now with a dark halo contribution given by an NFW profile. The top panel has the stellar M_*/L_I value from population models ($2.34 M_\odot/L_{\odot,I}$), and the bottom panel from the maximal disc model ($3.8 M_\odot/L_{\odot,I}$).

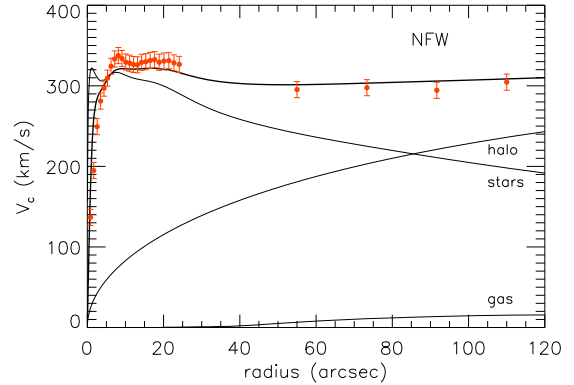


Figure 19. Best fit model of a dark halo with an NFW profile, with a concentration parameter $c = 10$ as indicated by cosmological simulation. This model has a stellar M/L of $3.3 M_\odot/L_{\odot,I}$. The red dots are the observations, and the black bold line the fit to these observations. The contributions of halo, stars and gas are plotted separately, where the first two curves are unconvolved.

Halo profile	M_*/L_I ($M_\odot/L_{\odot,I}$)	ρ_0, ρ_s ($M_\odot \text{ pc}^{-3}$)	r_c, r_s (kpc)	c	χ^2
Pseudo-isothermal	2.34	19	0.23	-	27
	3.8	0.06	5.4	-	133
NFW	2.34	1.1	2.1	71	44
	3.8	0.0011	130	4.7	144
	3.3	0.0067	38	10	87

Table 4. Comparison of the best fit models with a dark matter halo, as described in the text.

Modified Newtonian Dynamics (MOND, Milgrom 1983). In this theory, Newtonian dynamics is no longer valid for small accelerations ($a \ll a_0$), but instead the acceleration a in a gravitational field is given by

$$a\mu(a/a_0) = a_N, \quad (20)$$

where a_N is the Newtonian acceleration and μ is an interpolation function, such that $\mu(x) = 1$ for $x \gg 1$ and $\mu(x) = x$ for $x \ll 1$. Given the stellar mass-to-light ratio of a galaxy, MOND predicts its rotation curve. An overview of properties and predictions of MOND is offered by Sanders & McGaugh (2002).

We fitted our rotation curve of NGC 2974 with M_*/L_I as a free parameter. For a_0 we adopted the value of 1.2×10^{-8} cm/s², which was derived by Begeman, Broeils & Sanders (1991) from a sample of spiral galaxies. The contribution of the neutral gas is included in our model in the same way as described before, as well as a convolution to take seeing and sampling into account.

NGC 2974 is an ideal candidate to study the transition between the Newtonian and MOND regime, since the Newtonian acceleration reaches a_0 at a radius of approximately $95''$ if we adopt a stellar mass-to-light ratio of $2.34 M_\odot/L_{\odot,I}$. For larger M_*/L_I , this radius increases, and for the maximum disc value of $3.8 M_\odot/L_{\odot,I}$, a_0 is reached around $120''$. This means that a large part of the observed rotation curve lies in the transition region, and we could therefore use NGC 2974 to discriminate between interpolation function.

We first constructed a model with the standard interpolation function of MOND,

$$\mu(x) = \frac{x}{\sqrt{1+x^2}}. \quad (21)$$

The resulting fit is shown as model I in Figure 20. This model has the same M_*/L_I value as the maximal disc model, $3.8 M_\odot/L_{\odot,I}$, but does clearly not provide a good fit to the data.

We constructed a second model, with an alternative interpolation function explored by Famaey & Binney (2005),

$$\mu(x) = \frac{x}{1+x}. \quad (22)$$

This function makes the transition between the Newtonian and the MOND region less abrupt than the standard interpolation function and requires a lower M_*/L_I . The fit provided by this model to the data is much better (Model II in Figure 20), but formally less good than a model with a dark matter halo. This model requires $M_*/L_I = 3.6 M_\odot/L_{\odot,I}$, and the fit yields $\chi^2 = 98$, for 27-1 degrees of freedom.

Famaey & Binney (2005) find that their simple interpolation function provides better constraints to the terminal velocity of the Milky Way than the standard function. Famaey et al. (2007) fitted the rotation curves of a sample of galaxies with Hubble types ranging from small irregular dwarf galaxies to large early-type spirals, and report that both interpolating functions fit the data equally well. However, Sanders & Noordermeer (2007) find that for their sample of early-type disc galaxies the simple interpolation function yields more sensible values for M_*/L than the standard one.

It would be interesting to see whether there is a preference for the simple interpolation function over the standard one in early-type galaxies. In this scenario, the challenge

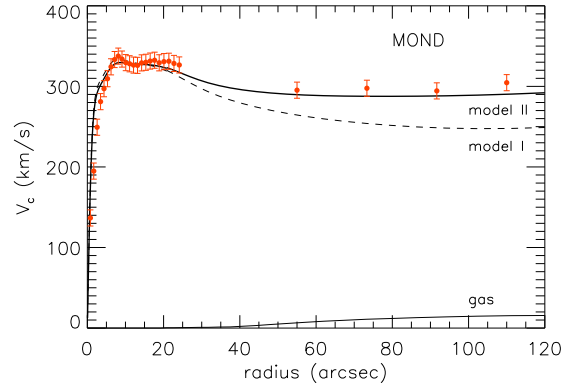


Figure 20. Observed rotation curve (red datapoints) and best fitting models with a MOND rotation curve. The dashed line (Model I) is constructed with the standard interpolation function, while the thick line (Model II) uses an alternative simple interpolation function (see text).

for MOND would be to provide a universal interpolation function that would fit rotation curves of all galaxy types along the Hubble sequence. So far, mostly spirals and dwarf galaxies have been confronted with MOND, but with more early-type galaxies getting detected in H I and more rotation curves becoming available, the sampling in morphology should become less biased to late-type galaxies.

6 SUMMARY

We obtained H I observations of the early-type galaxy NGC 2974 and found that the neutral gas resides in a ring. The ring starts around $50''$, and extends to $120''$, which corresponds to 12 kpc or 5 effective radii. The total mass of the neutral gas is $5.5 \times 10^8 M_\odot$.

We compared the velocity field of the H I ring with the kinematics of the ionised gas. We found that both velocity fields are very regular and nicely aligned, indicating that they could form a single disc. A harmonic decomposition of the velocity field showed that at large radii the gravitational potential is consistent with an axisymmetric shape.

We introduced a new way to correct the rotation curve of the ionised gas for asymmetric drift. We found that the correction approaches a constant value and this enabled us to remove the effect of turbulence on the rotation curve, assuming a constant asymmetric drift correction throughout the galaxy. We confirmed that this assumption is valid in NGC 2974, by comparing with the asymmetric drift corrected rotation curve of the stars (which was not affected by turbulence). An interesting question is whether other galaxies show the same behaviour. If this is the case, then with our method we would be able to investigate rotation curves of ionised gas and the effects of turbulence in more detail in other galaxies, and search for connections with e.g. spiral structure and bars. Although in principle we could for NGC 2974 also have used the stellar rotation curve together with the H I to constrain the mass models, this will not be the case for all galaxies. For instance, in low surface brightness galaxies stellar kinematics are not easy to obtain, and

even in high surface brightness galaxies, the absorption line kinematics need to be binned to higher signal-to-noise than the emission line kinematics, provided that ionised gas is present.

It is clear from the rotation curve of NGC 2974 that dark matter is required to explain the observed velocities. We found that the total mass-to-light ratio increases from $4.3 M_{\odot}/L_{\odot,I}$ at $1 R_e$ to $8.5 M_{\odot}/L_{\odot,I}$ at $5 R_e$. This last value would correspond to $14 M_{\odot}/L_{\odot,B}$ in *B*-band. Even in the maximal disc model, 55 per cent of the total mass is dark, and an additional dark halo needs to be included.

We constructed mass models of NGC 2974, where we modeled both the stellar and gaseous contribution to the gravitational potential. The latter is negligible compared to the stars ($M_{\text{gas}} \sim 0.001 M_*$), but still included in our models. For the dark halo, we tested two different profiles: the core-dominated pseudo-isothermal sphere and the cuspy NFW profile. We experimented with different values for the stellar mass-to-light ratio, but found that we cannot constrain this value with just the rotation curve: for most M_*/L smaller than the maximal disc value, we could obtain a decent fit for both the pseudo-isothermal sphere and the NFW profile. If we compare models with M_*/L_I from single stellar population models ($2.34 M_{\odot}/L_{\odot,I}$) with maximal disc model ($M_*/L_I = 3.8 M_{\odot}/L_{\odot,I}$), then the first provide better fits to the data. Especially the inner datapoints are better reproduced with $M_*/L_I = 2.34 M_{\odot}/L_{\odot,I}$, but we note that the H I data points are better fitted in the models with the larger M_*/L_I value. The pseudo-isothermal sphere fits our data marginally better than the NFW profile, but the difference is not significant. With MOND we can also reproduce the observed rotation curve, but not as well as with models that include a dark matter halo.

The largest uncertainty in our analysis is the stellar mass-to-light ratio. We can only derive an upper limit on this ratio from the maximal disc model or e.g. from Schwarzschild modeling, since M_*/L should always be equal to or smaller than the dynamical M/L . Values for M_*/L from stellar population synthesis models depend significantly on the model assumptions: we mentioned already that going from a Kroupa to a Salpeter IMF can increase M_*/L by as much as 40 per cent. Also, even low-level secondary star formation can affect M_*/L severely. Furthermore, there is no reason why the M_*/L should remain constant over 5 effective radii, which we assumed when modeling the stellar mass. If the stellar mass-to-light ratio were known, we would be able to determine the dark matter fraction in the galaxy with more accuracy, and either rule out or confirm the maximal disc hypothesis. Also, since M_*/L is the only free parameter when fitting a rotation curve in MOND, knowing this value would provide us with a rotation curve that can be compared to the data directly, providing a clear test for MOND.

We have shown in this paper that it is possible to combine rotation curves of neutral and ionised gas, correcting the latter one for asymmetric drift using the Jeans equations and the higher order velocity moments of the collisionless Boltzmann equations. Our method to correct for the asymmetric drift therefore does not require a cold disc assumption ($\sigma \ll V_c$). With more early-type galaxies getting detected in H I, and more high quality rotation curves be-

coming available, we can now study the shape of their dark matter haloes.

ACKNOWLEDGEMENTS

The authors would like to thank Martin Bureau, Michele Cappellari, Richard McDermid, Marc Sarzi and Scott Tremaine for useful discussions, and Remco van den Bosch for careful reading of the manuscript. We also are grateful to Jesús Falcón-Barroso for making available the MDM image of NGC 2974 prior to publication.

This research was supported by the Netherlands Research School for Astronomy NOVA, and by the Netherlands Organization of Scientific Research (NWO) through grant 614.000.426 (to AW). AW acknowledges The Leids Kerkhoven-Bosscha Fonds for contributing to working visits. GvdV acknowledges support provided by NASA through Hubble Fellowship grant HST-HF-01202.01-A awarded by the Space Telescope Science Institute, which is operated by the Association of Universities for Research in Astronomy, Inc., for NASA, under contract NAS 5-26555.

The Very Large Array is part of the National Radio Astronomy Observatory, which is a facility of the National Science Foundation operated under cooperative agreement by Associated Universities, Inc. The SAURON observations were obtained at the William Herschel Telescope, operated by the Isaac Newton Group in the Spanish Observatorio del Roque de los Muchachos of the Instituto de Astrofísica de Canarias.

The Digitized Sky Survey was produced at the Space Telescope Science Institute under US Government grant NAG W-2166. Photometric data of NGC 2974 was obtained using the 1.3-m McGraw-Hill Telescope of the MDM Observatory at Kitt Peak. We acknowledge the usage of the HyperLeda data base (<http://leda.univ-lyon1.fr>).

REFERENCES

- Bacon R., et al., 2001, MNRAS, 326, 23
- Begeman K.G., 1978, PhD thesis, Groningen University
- Begeman K.G., Broeils A.H., Sanders R.H., 1991, MNRAS, 249, 523
- Bertola F., Pizzella A., Persic M., Salucci P., 1993, ApJ, 416L, 45
- Binney J., Tremaine S., 1987, Galactic Dynamics, Princeton Univ. Press, Princeton, NJ
- Bregman J.N., Hogg D.E., Roberts M.S., 1992, ApJ, 387, 484
- Bridges T., et al., 2006, MNRAS, 373, 157
- Bullock J.S., Kolatt T.S., Sigad Y., Somerville R.S., Kravtsov A.V., Klypin A.A., Primack J.R., Dekel A., 2001, MNRAS, 321, 559
- Cappellari M., 2002, MNRAS, 333, 400
- Cappellari M., Verolme E.K., van der Marel R.P., Verdoes Kleijn G.A., Illingworth G.D., Franx M., Carollo C.M., de Zeeuw P.T., 2002, ApJ, 578, 787
- Cappellari M., et al., 2006, MNRAS, 366, 1126
- Catinella B., Giovanelli R., Haynes M.P., 2006, ApJ, 640, 751
- Cayatte V., Kotanyi C., Balkowski C., van Gorkom J.H., 1994, AJ, 107, 1003
- Casertano S., van Gorkom J.H., 1991, AJ, 101, 1231
- Cinzano P., van der Marel R.P., 1994, MNRAS, 270, 325
- de Blok W.J.G., 2005, ApJ, 634, 227
- de Blok W.J.G. & Bosma A., 2002, A&A, 385, 816
- Emsellem E., Goudfrooij P., Ferruit P., 2003, MNRAS, 345, 1297
- Emsellem E., et al., 2004, MNRAS, 352, 721

Emsellem E., et al., 2007, MNRAS, 2007, 379, 401
 Evans N.W., de Zeeuw P.T., 1994, MNRAS, 271, 202
 Famaey B., Binney J., 2005, MNRAS, 363, 603
 Famaey B., Gentile G., Bruneton J.-P., Hongsheng, 2007, PhRvD, 75, 3002
 Franx M., van Gorkom J.H., de Zeeuw P.T., 1994, ApJ, 436, 642
 Freedman W.L., et al., 2001, ApJ, 553, 47
 Gerhard O., Kronawitter A., Saglia R.P., Bender, R., 2001, AJ, 121, 1936
 Häring-Neumayer N., Cappellari M., Rix H.-W., Hartung M., Prieto M.A., Meisenheimer K., Lenzen R., 2006, ApJ, 643, 226
 Jeong H., Bureau M., Yi S.K., Krajnović D., Davies R.L., 2006, MNRAS, 2007, 376, 1021
 Kent S.M., de Zeeuw P.T., 1991, AJ, 102, 1994
 Kim D.-W., Jura M., Guhathakurta P., Knapp G.R., van Gorkom J.H., 1988, ApJ, 330, 684
 Krajnović D., Cappellari M., Emsellem E., McDermid R.M., de Zeeuw P.T., 2005, MNRAS, 357, 1113
 Krajnović D., Cappellari M., de Zeeuw P.T., Copin Y., 2006, MNRAS, 366, 787
 Kuijken K., Tremaine S., 1991, in Sundelius B., ed., Dynamics of Disc Galaxies. Göteborg Univ. Press, Göteborg, p.71
 Mei S., et al., 2005, ApJ, 625, 121
 Milgrom M., 1983, ApJ, 270, 365
 Morganti R., Sadler E.M., Oosterloo T., Pizzella A., Bertola F., 1997, AJ, 113, 937
 Morganti R. et al., 2006, MNRAS, 371, 157
 Navarro, J.F., Frenk C.S., White S.D.M., 1996, ApJ, 462, 563
 Noordermeer E., van der Hulst J.M., Sancisi R., Swaters R.S., van Albada T.S., 2007, MNRAS, 376, 1513
 Oosterloo T.A., Morganti R., Sadler E.M., Vergani D., Caldwell N., 2002, AJ, 123, 729
 Oosterloo T.A., Morganti R., Sadler E.M., van der Hulst T., Serra P., 2007, A&A, 465, 787
 Qian E.E., de Zeeuw P.T., van der Marel R.P., Hunter C., 1995, MNRAS, 274, 602
 Rix H.-W., de Zeeuw P.T., Cretton N., van der Marel R.P., Carollo C.M., 1997, ApJ, 488, 702
 Romanowsky A.J., Douglas N.G., Arnaboldi M., Kuijken K., Merrifield M.R., Napolitano N.R., Capaccioli M., Freeman K.C., 2003, Science, 301, 1696
 Sadler E.M., Oosterloo T.A., Morganti R., Karakas A., 2000, AJ, 119, 1180
 Sanders R.H., McGaugh S.S., 2002, ARA&A, 40, 263
 Sanders R.H., Noordermeer E., 2007, MNRAS, 379, 702
 Sarzi M., et al., 2006, MNRAS, 366, 1151
 Sault, R.J., Teuben, P.J., Wright, M.C.H. 1995, in ADASS IV, ed. R. Shaw, H.E. Payne, J.J.E. Hayes, ASP Conf. Ser., 77, 433,
 Schoenmakers R.H.M., 1998, ASPC, 136, 240
 Schoenmakers R.H.M., Franx M., de Zeeuw P.T., 1997, MNRAS, 292, 349
 Serra P., Trager S.C., van der Hulst J.M., Oosterloo T.A., Morganti R., 2006, A&A, 453, 493
 Spekkens K., Giovanelli R., 2006, AJ, 132, 1426
 Tonry J.L., Dressler A., Blakeslee J.P., Ajhar E.A., Fletcher A.B., Luppino G.A., Metzger M.R., Moore C.B., 2001, ApJ, 546, 681
 van Albada T.S., Bahcall J.N., Begeman K., Sancisi R., 1985, ApJ, 295, 305
 van der Kruit P.C., Allen R.J., 1978, ARA&A, 16, 103
 van den Bosch F.C., Robertson B.E., Dalcanton J.J., de Blok W.J.G., 2000, AJ, 119, 1579
 Weldrake D.T.F., de Blok W.J.G., Walter F., 2003, MNRAS, 340, 12

APPENDIX A: ASYMMETRIC DRIFT CORRECTION IN A THIN DISC

In this appendix we derive expressions for the asymmetric drift correction in a stationary axisymmetric system, using the velocity moments of the collisionless Boltzmann equation. We then evaluate this expression in a thin disc approximation. Our method does not require that the velocity dispersion should be small compared to the circular velocity ($\sigma/V_c \ll 1$) and is comparable to the “hot disc model”, (see e.g. Häring-Neumayer et al. 2006).

A1 The velocity ellipsoid

To derive the asymmetric drift correction we start from the collisionless Boltzmann equation for a stationary axisymmetric galaxy and using cylindrical coordinates $\vec{r} = (R, \phi, z)$,

$$v_R \frac{\partial f}{\partial R} + v_z \frac{\partial f}{\partial z} + \left(\frac{v_\phi^2}{R} - \frac{\partial \Phi}{\partial R} \right) \frac{\partial f}{\partial v_R} - \frac{v_R v_\phi}{R} \frac{\partial f}{\partial v_\phi} - \frac{\partial \Phi}{\partial z} \frac{\partial f}{\partial v_z} = 0, \quad (\text{A1})$$

with $f(R, z; v_R, v_\phi, v_z)$ the distribution function, $\Phi(R, z)$ the underlying potential and $\nu(\vec{r})$ the (luminosity) density given by $\int f(\vec{r}; \vec{v}) d\vec{v}$. We multiply the above equation by v_R and subsequently integrate over all velocities. We then obtain the Jeans equation:

$$\frac{\partial(\nu \overline{v_R^2})}{\partial R} + \frac{\partial(\nu \overline{v_R v_z})}{\partial z} + \frac{\nu}{R} \left(\overline{v_R^2} - \overline{v_\phi^2} + R \frac{\partial \Phi}{\partial R} \right) = 0. \quad (\text{A2})$$

Since our system is axisymmetric, we set $\partial \nu / \partial z = 0$ by symmetry. Substituting the circular velocity $V_c^2 = R(\partial \Phi / \partial R)$, we arrive at Equation (4-33) of Binney & Tremaine (1987):

$$V_c^2 = \overline{v_\phi^2} - \sigma_R^2 \left[\frac{\partial \ln \nu}{\partial \ln R} + \frac{\partial \ln \sigma_R^2}{\partial \ln R} + 1 - \frac{\sigma_\phi^2}{\sigma_R^2} + \frac{R}{\sigma_R^2} \frac{\partial(\overline{v_R v_z})}{\partial z} \right], \quad (\text{A3})$$

with $\sigma_\phi^2 = \overline{v_\phi^2} - \overline{v_\phi}^2$, $\sigma_R^2 = \overline{v_R^2}$ and $\sigma_z^2 = \overline{v_z^2}$. The observed velocity field gives $\overline{v_\phi}$, and the remaining terms in Equation (A3) form the asymmetric drift correction.

The last term in the asymmetric drift correction depends on the alignment of the velocity ellipsoid. In case of alignment with the cylindrical coordinate system (R, ϕ, z) we have $\overline{v_R v_z} = 0$, while in case of alignment with the spherical coordinate system (r, θ, ϕ) we have $\overline{v_R v_z} = (\sigma_R^2 - \sigma_z^2)(z/R)/[1 - (z/R)^2]$, which becomes proportional to z/R close to the disc plane. These are two extreme situations, and we introduce the parameter κ to find a compromise:

$$\overline{v_R v_z} = \kappa(\sigma_R^2 - \sigma_z^2) \frac{z/R}{1 - (z/R)^2}, \quad 0 \leq \kappa \leq 1, \quad (\text{A4})$$

where a typical value for κ is 0.5 for disc galaxies (e.g. Kent & de Zeeuw 1991).

To evaluate the asymmetric drift correction, we need expressions for σ_ϕ/σ_R and σ_z/σ_R . We use higher order velocity moments of the collisionless Boltzmann equation to derive these expressions.

Starting again from Equation (A1), we multiply by $v_R v_\phi$ and integrate over all velocities:

$$\frac{\partial(\nu \overline{v_R^2 v_\phi})}{\partial R} + \frac{\partial(\nu \overline{v_R v_z v_\phi})}{\partial z} + \frac{\nu}{R} \left(2\overline{v_R v_\phi} - \overline{v_\phi^2} - \overline{v_\phi} R \frac{\partial \Phi}{\partial R} \right) = 0. \quad (\text{A5})$$

Aligning the velocity ellipsoid in the azimuthal direction we have $\overline{v_R^2 (v_\phi - \overline{v_\phi})} = 0$ and $\overline{v_R v_z (v_\phi - \overline{v_\phi})} = 0$, so that $\overline{v_R^2 v_\phi} = \sigma_R^2 \overline{v_\phi}$ and $\overline{v_R v_z v_\phi} = \overline{v_R v_z} \overline{v_\phi}$. We substitute these

relations in Equation (A5), and subtract $\overline{v_\phi}$ times the Jeans equation (A2):

$$\nu \sigma_R^2 \frac{\partial \overline{v_\phi}}{\partial R} + \nu \overline{v_r v_z} \frac{\partial \overline{v_\phi}}{\partial z} + \frac{\nu}{R} \left[\sigma_R^2 \overline{v_\phi} - (\overline{v_\phi^3} - \overline{v_\phi^2 \overline{v_\phi}}) \right] = 0. \quad (\text{A6})$$

We substitute $\overline{v_\phi^3} - \overline{v_\phi^2 \overline{v_\phi}} = 2\sigma_\phi^2 \overline{v_\phi} + (\overline{v_\phi - \overline{v_\phi}})^3$ and $\overline{v_r v_z}$ from Equation (A4) to arrive at

$$\frac{\sigma_\phi^2}{\sigma_R^2} = \frac{1}{2} \left(1 + \alpha_R + \kappa \frac{1 - \sigma_z^2/\sigma_R^2}{1 - (z/R)^2} \alpha_z - \frac{(\overline{v_\phi - \overline{v_\phi}})^3}{\sigma_R^2 \overline{v_\phi}} \right), \quad (\text{A7})$$

where we have introduced the logarithmic slopes

$$\alpha_R = \frac{\partial \ln \overline{v_\phi}}{\partial \ln R}, \quad \text{and} \quad \alpha_z = \frac{\partial \ln \overline{v_\phi}}{\partial \ln z}. \quad (\text{A8})$$

To obtain an expression for σ_z/σ_R we again start with the collisionless Boltzmann equation, but now multiply with $v_z(v_\phi - \overline{v_\phi})$ before integrating over all velocities:

$$\nu \overline{v_r v_z} \frac{z}{R} \left(1 + \frac{\partial \ln \overline{v_\phi}}{\partial \ln R} \right) + \nu \sigma_z^2 \frac{\partial \ln \overline{v_\phi}}{\partial \ln z} = 0. \quad (\text{A9})$$

Substituting Equation (A4) we find

$$\frac{\sigma_z^2}{\sigma_R^2} = \frac{\kappa z^2 (1 + \alpha_R)}{\kappa z^2 (1 + \alpha_R) - (R^2 - z^2) \alpha_z}, \quad (\text{A10})$$

The above expressions can be inserted into Equation (A3) to obtain the asymmetric drift correction and therefore the true circular velocity. In practice, we often apply the asymmetric drift correction in the thin disc approximation, because from observations the z -dependence is not straightforward to derive.

In the thin disc approximation, we have $z \ll R$, and therefore we can write Equation (A4) as

$$\overline{v_r v_z} = \kappa (\sigma_R^2 - \sigma_z^2) \frac{z}{R}. \quad (\text{A11})$$

and following the same reasoning as before, we see that the expressions in Equations (A7) and (A10) simplify slightly: in the first expression the one-to-last term disappears, and for the second one, $(R^2 - z^2)$ gets replaced by R^2 in the nominator of the expression. Furthermore, the derivative of $\overline{v_r v_z}$ simplifies considerably.

We find the following expression for the asymmetric drift correction in the thin disc approximation, after substitution in Equation (A3):

$$V_c^2 = \overline{v_\phi^2} - \sigma_R^2 \left[\frac{\partial \ln \nu}{\partial \ln R} + \frac{\partial \ln \sigma_R^2}{\partial \ln R} + \frac{1}{2} (1 - \alpha_R) + \frac{1}{2} \frac{(\overline{v_\phi - \overline{v_\phi}})^3}{\sigma_R^2 \overline{v_\phi}} - \frac{\kappa R^2 \alpha_z}{\kappa z^2 (1 + \alpha_R) - R^2 \alpha_z} \right]. \quad (\text{A12})$$

The one-to-last term vanishes in the case of a velocity ellipsoid symmetric around $v_\phi = \overline{v_\phi}$. This need not necessarily be the case, and the exact form of $(\overline{v_\phi - \overline{v_\phi}})^3$ depends on the underlying distribution function, which in general cannot be constrained easily (e.g. Kuijken & Tremaine 1991). However, since this term is a factor σ_R^2 smaller than the other terms, it can be safely ignored for most purposes.

A2 Observables

Here we investigate how in the thin disc approximation we can correct our observed velocity field for asymmetric drift,

to obtain the true circular velocity V_c . This quantity traces the potential and therefore the mass of the galaxy.

In a thin disc, we can replace $\partial \ln \nu / \partial \ln R$ by the slope of the surface brightness $\partial \ln \Sigma / \partial \ln R$. This slope can be obtained directly from observations.

The observed velocity and velocity dispersion of an axisymmetric thin disc seen under an inclination i is given by:

$$\begin{aligned} V &= v_{\text{sys}} + \overline{v_\phi} \cos \phi \sin i, \\ \sigma^2 &= \sigma_R^2 \sin^2 \phi \sin^2 i + \sigma_\phi^2 \cos^2 \phi \sin^2 i + \sigma_z^2 \cos^2 i \\ &\quad - \overline{v_r v_z} \sin \phi \sin 2i. \end{aligned} \quad (\text{A13})$$

It is straightforward to obtain $\overline{v_\phi}$ from the observed velocity field, and though α_R can be estimated rather well, α_z is less easy to constrain. Therefore, we fit to $\overline{v_\phi}$ the prescription of Evans & de Zeeuw (1994) for power-law models:

$$v_{\text{mod}} \propto \frac{R}{(R_c^2 + R^2 + z^2/q_\Phi^2)^{1/2 + \beta/4}}, \quad (\text{A14})$$

where R_c is the core radius, q_Φ the flattening of the potential and β the logarithmic slope of the rotation curve at large radii (such that $\beta = 0$ implies a flat rotation curve).

For the slopes of $\overline{v_\phi}$ we find that:

$$\begin{aligned} \alpha_R &= 1 - \frac{(1 + \beta/2) R^2}{R_c^2 + R^2 + z^2/q_\Phi^2} \\ \alpha_z &= -\frac{(1 + \beta/2) z^2/q_\Phi^2}{R_c^2 + R^2 + z^2/q_\Phi^2} = -\frac{z^2}{q_\Phi^2 R^2} (1 - \alpha_R), \end{aligned} \quad (\text{A15})$$

so that with $\overline{v_r v_z} = 0$ in the disc plane, we obtain:

$$\sigma^2 = \sigma_R^2 \left[1 - \frac{1}{2} (1 - \alpha_R) \cos^2 \phi \sin^2 i - \frac{(1 + \beta/2) R^2}{\kappa q_\Phi^2 (R_c^2 + R^2) (1 + \alpha_R) + (1 + \beta/2) R^2} \cos^2 i \right]. \quad (\text{A16})$$

When evaluated along the major axis, $\cos^2 \phi = 1$.

Assuming that the velocity ellipsoid is symmetric around $v_\phi = \overline{v_\phi}$ the corresponding term in Equation (A12) vanishes. Inserting the relations obtained from the power-law model, we arrive at the following expression for the circular velocity:

$$V_c^2 = \overline{v_\phi^2} - \sigma_R^2 \left[\frac{\partial \ln \Sigma}{\partial \ln R} + \frac{\partial \ln \sigma_R^2}{\partial \ln R} + \frac{1}{2} (1 - \alpha_R) + \frac{\kappa (1 - \alpha_R)}{\kappa (2R_c^2 - R^2) + R^2} \right]. \quad (\text{A17})$$